Earth Planet. Sci. Lett. 630 (2024) 118623

Contents lists available at ScienceDirect

Earth and Planetary Science Letters

journal homepage: www.elsevier.com/locate/epsl

Cenozoic stable isotope constraints on the Eurasian continental interior hydroclimate response to high CO_2

Ellie Driscoll [a], Michael R. Needham [b], Patrick W. Keys [b], Jeremy K.C. Rugenstein [a,*]

[a] Department of Geosciences, Colorado State University, Fort Collins, CO 80523, United States
[b] Department of Atmospheric Science, Colorado State University, Fort Collins, CO 80521, United States

ARTICLE INFO

Keywords:
Stable isotopes
Hydroclimate
Eurasia
Cenozoic
Climate models

ABSTRACT

The response of the terrestrial hydrologic cycle to higher atmospheric CO_2 remains poorly constrained, largely due to difficulty in predicting how land surface processes may modify individual hydroclimate parameters such as precipitation (P), evapotranspiration (ET), and runoff (q). To interrogate how the terrestrial hydrologic cycle may change with warming and higher CO_2, we utilize the Cenozoic geologic record of terrestrial stable oxygen isotopes ($\delta^{18}O$) as recorded in authigenic minerals, which reflect precipitation $\delta^{18}O$ ($\delta^{18}O_p$). Values of $\delta^{18}O_p$ are sensitive to changes in terrestrial hydroclimate, including to the ratio of P/ET and to precipitable water. In short, decreasing P/ET or higher precipitable water produces shallower $\delta^{18}O_p$ gradients inland, whereas increasing P/ET or lower precipitable water results in steeper $\delta^{18}O_p$ continental gradients. We compile nearly 15,000 samples of authigenic carbonate and tooth enamel across Eurasia—the largest continental landmass—that span the Cenozoic Era to reconstruct the past spatial distribution and zonal (*i.e.* east-to-west) gradients of $\delta^{18}O_p$. We find that, in epochs with higher CO_2, zonal $\delta^{18}O_p$ gradients increase, suggesting an increase in P/ET across Eurasia despite the expected increase in precipitable water in greenhouse climates. We compare these results to $\delta^{18}O_p$ gradients simulated by an isotope-enabled climate model (iCESM) forced with both pre-industrial (PI) and 4xPI CO_2 mixing ratios. Simulated $\delta^{18}O_p$ gradients shallow as CO_2 rises, in contrast to the reconstructed $\delta^{18}O_p$ gradients. This data-model mismatch suggests either that Earth system feedbacks not represented in our iCESM simulations, such as changes in Northern Hemisphere ice extent and vegetation, may have fundamentally changed Northern Hemisphere hydroclimate or that land-surface processes under high CO_2 climates may be misrepresented in iCESM.

1. Introduction

Projections of the terrestrial water cycle response to higher atmospheric CO_2 remain uncertain because the terrestrial water cycle is defined by several interacting components, including precipitation (P), evapotranspiration (ET), and runoff (q), each of which may change independently with warming (Scheff et al., 2022, 2017; Swann et al., 2016). This uncertainty partly arises because the land surface plays a critical role in modifying the hydrological cycle (Mankin et al., 2018; Swann et al., 2016). The land surface, unlike the ocean, is not well-watered, meaning that in many places, ET is restricted by water availability rather than available energy. Further complicating the response of the terrestrial hydrological cycle to warming is the role of plants, which use water (*i.e.,* transpiration) to fix CO_2 into organic carbon. The precise physiological response of plants to higher CO_2—modulated by trade-offs between CO_2 fertilized biomass growth and decreasing stomatal conductance—will partly determine how global transpiration changes in response to higher CO_2 (Lemordant et al., 2018; Medlyn et al., 2011; Yang et al., 2019). However, predicting how plants and terrestrial ecosystems will respond to warming remains subject to considerable uncertainty; yet, this response will determine how much P is partitioned to ET or to q (Fisher et al., 2019; Lemordant et al., 2018; Mankin et al., 2018; Scheff et al., 2017). Lastly, though precipitation is likely to increase at the global-sale, models disagree on the amplitude, temporal distribution, and even the sign of regional changes (Douville et al., 2021; Scheff et al., 2022, 2017). The sum of these uncertainties and how they interact as CO_2 rises makes predicting the response of the terrestrial hydrological cycle to warming difficult to constrain with models.

We use the paleoclimate record to evaluate how the terrestrial water

* Corresponding author.
E-mail address: jeremy.rugenstein@colostate.edu (J.K.C. Rugenstein).

https://doi.org/10.1016/j.epsl.2024.118623
Received 14 September 2023; Received in revised form 4 February 2024; Accepted 11 February 2024

cycle will change as CO_2 rises, focusing on periods of extended warmth and high CO_2 during the Cenozoic Era. To constrain past hydroclimate, we use the stable isotopes of oxygen ($\delta^{18}O$) as preserved in calcium carbonate and tooth enamel, which reflect past precipitation $\delta^{18}O$. Precipitation $\delta^{18}O$ ($\delta^{18}O_p$) is particularly sensitive to the relationship between P, ET, and q. As moisture is transported over land, P preferentially removes ^{18}O from atmospheric water vapor, whereas ET generally resupplies the atmosphere with ^{18}O (Rozanski et al., 1993; Winnick et al., 2014). Consequently, the rate of decrease of $\delta^{18}O_p$ over land along a prevailing storm track (what we term the $\delta^{18}O$ gradient, following McDermott et al. (2011)) reflects the ratio of P to ET (and by extension q) and therefore net rainout (Kukla et al., 2019; Winnick et al., 2014). In areas with high net rainout (high P/ET), $\delta^{18}O_p$ decreases rapidly inland; in contrast, in regions with high ET relative to P (low P/ET), $\delta^{18}O_p$ decreases only slightly, even over vast distances (Winnick et al., 2014).

In this study, we build upon work by McDermott et al. (2011), who examined zonal gradients in Holocene speleothem $\delta^{18}O$ across Europe. McDermott et al. (2011) demonstrated substantial changes in past $\delta^{18}O_p$ gradients over Europe in just the past 12 ka, though the precise mechanism remained elusive. We extend this work by reconstructing zonal gradients of past $\delta^{18}O_p$ across the Eurasian continental interior over the Cenozoic to isolate the effect of warming and high CO_2 on terrestrial hydroclimate. The continental interior of Eurasia provides a particularly favorable study region as it is the largest continental landmass on Earth and, north of the major Eurasian monsoonal systems, is largely dominated by a single air mass, with moisture transport from Europe to Asia driven by the westerlies (Numaguti, 1999; Rugenstein and Chamberlain, 2018). Indeed, much of the precipitation that falls over interior Asia is sourced from evaporated or transpired continental moisture from Europe (Numaguti, 1999; van der Ent et al., 2010), permitting us to isolate the effects of higher CO_2 on terrestrial hydroclimate.

Today, these effects lead to a progressive decrease in $\delta^{18}O_p$ eastward across interior Eurasia—indeed, this observation originally inspired the term "continental effect" (Rozanski et al., 1993). Kurita et al. (2004) demonstrated that this decrease in $\delta^{18}O_p$ is intimately linked to P/ET: in summer, low P/ET ratios result in a shallow $\delta^{18}O_p$ gradient across interior Eurasia, whereas winter—with negligible ET and thus high P/ET—is characterized by a steep $\delta^{18}O_p$ gradient. We take advantage of this well-studied zonal $\delta^{18}O_p$ gradient and examine whether and how this zonal gradient has varied in the past in response to changing CO_2. We find that, during periods of warmer temperatures and higher CO_2 in the Cenozoic, the zonal $\delta^{18}O_p$ gradient steepens, driven by higher past $\delta^{18}O_p$ in Europe.

We additionally compare the results of our reconstructed zonal $\delta^{18}O_p$ gradients to projected changes in $\delta^{18}O_p$ gradients at higher CO_2 as simulated by an isotope-enabled Earth System Model (iCESM). The steepest zonal $\delta^{18}O_p$ gradient across Eurasia in iCESM occurs with pre-industrial CO_2, whereas our geologic data indicate the steepest gradients during epochs of elevated CO_2. We suggest that this model-data discrepancy arises either from mis-representations of the processes that generate runoff in climate models—such as the temporal distribution of precipitation—or from Earth system feedbacks not represented in our model experiments such as ice sheet decay and boreal forest expansion at high CO_2 that may change the relationship between proxy $\delta^{18}O$ and $\delta^{18}O_p$.

2. Background

2.1. Oxygen isotope systematics

As an air mass travels inland, precipitation progressively removes ^{18}O, resulting in characteristically low inland $\delta^{18}O_p$, often referred to as the "continental effect" (Araguás-Araguás et al., 1998; Rozanski et al., 1993; Winnick et al., 2014). However, ET typically returns high $\delta^{18}O_p$ moisture due either to the predominance of transpiration, which largely does not fractionate ^{18}O (Kurita et al., 2004; Winnick et al., 2014), or to quantitative recycling of moisture to the atmosphere (Caves et al., 2015; Feng et al., 2013). Thus, the $\delta^{18}O_p$ gradient along a single storm track reflects the degree of net rainout (P/ET), with net rainout values near zero shallowing the $\delta^{18}O_p$ gradient, whereas high values of P/ET—such as across major mountain ranges—result in a steep $\delta^{18}O_p$ gradient (Caves et al., 2015; Kukla et al., 2019; Winnick et al., 2014).

As CO_2 rises, $\delta^{18}O_p$ is also impacted by the thermodynamic response of the atmosphere to warming (van Dijk et al., 2020; Winnick et al., 2015). Because precipitable water increases at approximately 7%/K, but global P (and ET) only increases at ~2%/K (Held and Soden, 2006; Pendergrass and Hartmann, 2014), the total reservoir of atmospheric moisture increases. This effect alone dampens changes in $\delta^{18}O_p$, causing decreases in both zonal and meridional gradients of $\delta^{18}O_p$ (Kukla et al., 2019; van Dijk et al., 2020).

This $\delta^{18}O_p$ is recorded in a variety of authigenic materials, including authigenic carbonates and tooth enamel (Breecker et al., 2009; Koch, 2007; Leng and Marshall, 2004; McDermott et al., 2011). Carbonate $\delta^{18}O$ ($\delta^{18}O_c$) is related to $\delta^{18}O_p$—assuming isotopic equilibrium during formation—via a temperature-dependent fractionation (Kim and O'Neil, 1997), though the sensitivity of this fractionation to temperature changes is small at Earth surface temperatures (~0.22‰/°C). Tooth enamel $\delta^{18}O$ ($\delta^{18}O_e$) reliably records the $\delta^{18}O$ of an animal's primary water source and reflects oxygen uptake and loss during tooth development (Domingo et al., 2013; Kohn, 1996). Reconstructions of past $\delta^{18}O_p$ from mammal $\delta^{18}O_e$ offer different complications from that of $\delta^{18}O_c$. Although the internal regulation of body temperature alleviates uncertainty of mineral formation temperature by generating a constant offset between body-water $\delta^{18}O$ ($\delta^{18}O_{bw}$) and $\delta^{18}O_e$, physiological factors affect $\delta^{18}O_{bw}$ by altering the magnitude of inward and outward oxygen fluxes (Domingo et al., 2013; Koch, 2007). Due to these physiological differences, various taxa-specific conversions from $\delta^{18}O_e$ to $\delta^{18}O_p$ have been established for modern mammals and estimates of past $\delta^{18}O_p$ often rely on comparison to the closest living relative of the fossil taxa (Domingo et al., 2013).

Using $\delta^{18}O_{c/e}$ as a tracer of past or present $\delta^{18}O_p$ and hence P/ET is complicated by a variety of processes that modify $\delta^{18}O_{c/e}$ largely independent of P or ET. For example, mixing of air masses with different moisture sources and therefore different $\delta^{18}O$ can change $\delta^{18}O_p$ (Araguás-Araguás et al., 1998; Caves et al., 2015; Feng et al., 2013; McDermott et al., 2011). Topography also modifies $\delta^{18}O_p$ due to orographic precipitation (Campani et al., 2012; San Jose et al., 2020); thus, changes in past $\delta^{18}O_p$ may be due to changes in orography, rather than a hydroclimatic response to higher CO_2. Changes in temperature, evaporation, and diagenesis (Garzione et al., 2004; Leng and Marshall, 2004; Methner et al., 2020) can further decouple $\delta^{18}O_{c/e}$ from past $\delta^{18}O_p$. These complicating effects can often be identified and quantified by accounting for the spatial distribution of past $\delta^{18}O_p$, which permit attribution of shifts in $\delta^{18}O_{c/e}$ to changes in air mass mixing, local/regional topographic changes, temperature, diagenesis, or to global changes in CO_2 (Caves et al., 2015; Kukla et al., 2022b; Liu et al., 2010; McDermott et al., 2011; Rugenstein and Chamberlain, 2018).

2.2. Modern Eurasian continental interior hydroclimate

Precipitation generally decreases eastward in the interior of Eurasia (Meyer-Christoffer et al., 2015; Oshima et al., 2015), though there are local precipitation maxima associated with topography. Precipitation is high in south and east Asia because of the South and East Asian Monsoons (Fig. 1A,B). In contrast to the gradual decrease in precipitation eastward across interior Eurasia, precipitation seasonality has a sharp boundary coincident with major ranges in interior Asia around 70–80° E (Baldwin and Vecchi, 2016; Caves et al., 2017). Whereas most of interior Eurasia receives much of its annual rainfall between September and May—particularly in and around the Mediterranean and to the east in Arabia—most of interior Asia receives much of its rainfall in the summer

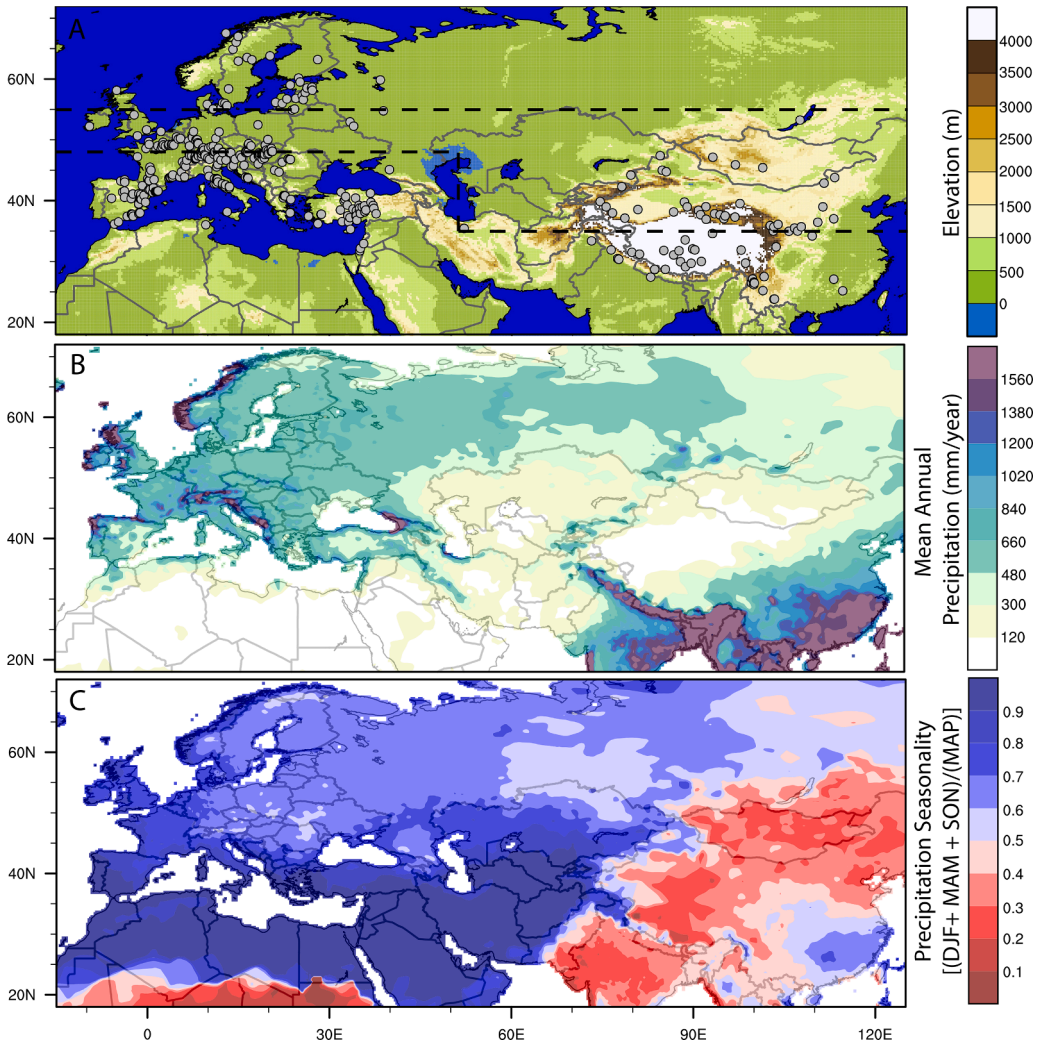

Fig. 1. (A) Topographic map of Eurasia. Gray points are all sampling sites in our compilation. Dashed black lines indicate the spatial extent of the filtered data used in calculating the zonal $\delta^{18}O_p$ gradient. (B) Mean annual precipitation (MAP) (mm/year) derived from the Global Precipitation Climatology Project (GPCP) (Meyer-Christoffer et al., 2015). Darker colors are higher precipitation amounts; lighter colors are lower precipitation amounts. (C) Precipitation seasonality, defined as the fraction of precipitation that falls between September and May over the total amount of precipitation, using GPCP data. Bluer colors indicate that the majority of precipitation falls between September and May; redder colors indicate that the majority of precipitation falls during the summer (JJA).

months (June, July, and August (JJA)) (Fig. 1C). This stark seasonality contrast has been attributed to the presence of the Siberian High in interior Asia that suppresses winter precipitation (Aizen et al., 2001; Oshima et al., 2015) as well as high topography in interior Asia that forces orographic precipitation during the migration of the mid-latitude jet in spring and fall (Baldwin and Vecchi, 2016; Caves et al., 2017).

The Eurasian continental interior is linked hydroclimatically via the mid-latitude westerlies. The precipitation that falls in western Eurasia during the winter is evapo-transpired the following spring and summer, where it is transported downwind to interior Asia, precipitating in the summer (Numaguti, 1999; Oshima et al., 2015; Yatagai and Yasunari, 1998). Thus, interior Asia is a major sink for continental precipitation that originated further west in Eurasia (van der Ent et al., 2010; Wang et al., 2017). The strength of this westerlies link across Eurasia varies with latitude due to the influence of topography and variable moisture sources in both Europe and Asia. The Mediterranean region receives moisture dominantly from the Mediterranean (Gat and Carmi, 1970). Further east, the Asian monsoonal systems transport large quantities of water northward, though the northward extent of this moisture transport is limited by the major east-west Tethyan mountain ranges in southern Eurasia—including the Hindu Kush, Pamir, and Himalayas (Araguás-Araguás et al., 1998; Caves et al., 2015; Rugenstein and Chamberlain, 2018). North of these ranges, westerly moisture—originating originally in the North Atlantic—dominates the moisture budget (Araguás-Araguás et al., 1998; Numaguti, 1999; Yatagai and Yasunari, 1998).

3. Methods

3.1. Compilation of proxy data

We compiled data from 143 total publications that span the Cenozoic Era, with 57 publications based on samples collected in Europe and 86 from Asia, totaling 14,810 unique samples (Table S3) and archived in the PATCH Lab (Kukla et al., 2022a). Although the compilation includes samples from the Paleocene epoch, the subsequent discussion only examines data through the Eocene, as there are few Paleocene data. This compilation predominantly includes data from calcite proxies, including paleosol, lacustrine, and speleothem carbonate and mammal tooth enamel carbonate, though there is also tooth enamel phosphate data (n = 687 of 1178 enamel samples) from a diverse suite of taxa. Data from each study was screened for indications of evaporative enrichment or diagenetic alteration. Lacustrine datasets with positive covariation between $\delta^{13}C$ and $\delta^{18}O$ were presumed to be evaporatively impacted and

only the lowest 20% of values were used in site-averages from those localities (Li et al., 2015) (see also section 5.1.1). Data that the original studies highlighted as being potentially diagenetically altered were not included.

We also compiled modern meteoric water $\delta^{18}O$ ($\delta^{18}O_{mw}$) data (n = 64,000) across Eurasia, including precipitation, river/stream water, groundwater, and tap water $\delta^{18}O$, using the International Atomic Energy Agency's Global Network of Isotopes in Precipitation/Rivers database (IAEA/WMO, 2020a, 2020b), the Waterisotopes.org database, and select studies (see Table S4 for full list of references). We compile and analyze all of these water types because $\delta^{18}O_p$ data remains relatively sparse across much of interior Eurasia; however, river and stream waters, groundwater, and tap water integrate across storm events and frequently reflect long-term average $\delta^{18}O_p$ (Rugenstein and Chamberlain, 2018; San Jose et al., 2020), thereby providing a long-term $\delta^{18}O_p$ average across interior Eurasia.

3.2. Conversion of proxy $\delta^{18}O$ to past precipitation $\delta^{18}O$ ($\delta^{18}O_{pp}$)

To directly compare $\delta^{18}O$ across proxy types and with $\delta^{18}O_{mw}$, we convert $\delta^{18}O_{c/e}$ to an estimated past $\delta^{18}O_p$. For $\delta^{18}O_c$, we use interpolated modern June-July-August (JJA) surface air temperatures for each sample location from reanalysis data (NCEP-DOE AMIP-II Reanalysis; Kanamitsu et al. (2002)) and adjust for estimated temperature differences in the past relative to the modern using Cenozoic temperature estimates from benthic foraminifera (Lear et al., 2000). We use JJA surface air temperatures under the assumption that most authigenic carbonates (*i.e.*, paleosol and lacustrine carbonates) in our compilation form during the summer months (Breecker et al., 2009). We also test the sensitivity of our results to the assumption of JJA temperatures by comparing our results with both mean annual temperatures and a spatially constant temperature (Figs. S12–14). We use these estimated paleo-surface temperatures to calculate the ^{18}O fractionation between water and calcite (Kim and O'Neil, 1997). For $\delta^{18}O_e$ data, we use previously published mammal-specific $\delta^{18}O_e - \delta^{18}O_{mw}$ equations where possible. If no equation exists for a specific species or group, then a general equation calibrated for all mammals was used (Amiot et al., 2004). In cases where only the carbonate component of the tooth enamel was reported, we use a general $\delta^{18}O_c - \delta^{18}O_{mw}$ equation (Zanazzi et al., 2007).

3.3. HYSPLIT modeling

Since $\delta^{18}O_p$ is affected by air mass mixing, we use HYSPLIT—a model that tracks air parcels backward in time and space from a given location (Stein et al., 2015)—to understand which sites receive dominantly westerly moisture versus a mixture of westerly and non-westerly moisture. Air parcel trajectories were tracked backwards from a gridded set of locations (n = 63) across a latitudinal range of 30°N to 55°N and a longitudinal range of 0°E to ~100°E (Fig. 2). We use output from the Global Data Assimilation System (GDAS) with 1° x 1° resolution to calculate 168-hour back trajectories every 6 h from 2005 to 2016. At each location, we initialized trajectories at 1500 m above ground level, totaling 17,088 trajectories per site. Though HYSPLIT does not strictly track moisture, comparison with the Water Accounting Model 2-layers (see Supplemental Material Section 4; Fig. S2) demonstrates that across interior Eurasia, HYSPLIT approximates moisture sources well. We also provide seasonal HYSPLIT maps in the supplement (Fig. S3-S4)

3.4. Data filtering

To perform statistical tests on our $\delta^{18}O$ data and limit our analysis to only sites that have likely received dominantly westerly moisture, we limit the latitudinal range of both the modern and paleoclimate data used in our analysis, based on the results of the HYSPLIT modeling. West of 50°E (Europe), we include only samples between 47°N-55°N; east of 50°E (Asia), we include only data between 35°N-55°N (the northernmost proxy sample in Asia is 55°N). When analyzing modern $\delta^{18}O_{mw}$, we restrict our analysis to these same latitudinal bands. Hereafter, this limited dataset is referred to as the "filtered" dataset.

For the filtered dataset, we calculate average past $\delta^{18}O_p$ values for both Europe and Asia in each epoch and perform a student's t-test on the mean values to determine whether differences between Europe and Asia are significant (see boxplots in Fig. S11). To visualize and calculate the magnitude of the decrease in past $\delta^{18}O_p$ in different epochs, we present the data against longitude and calculate the slope of the past zonal $\delta^{18}O_p$ profile using a linear best-fit. Although the actual decrease in $\delta^{18}O_p$ across interior Eurasia does not change linearly (Fig. 3B), we use this linear approximation as it requires the fewest assumptions regarding the shape of the zonal $\delta^{18}O_p$ gradient. More complex formulations would require more data to further constrain the shape of the gradient. We utilize two methods to compare past zonal $\delta^{18}O_p$ gradients between epochs: 1) by determining the confidence interval at which the two slopes do not overlap, and 2) by calculating the significance of the

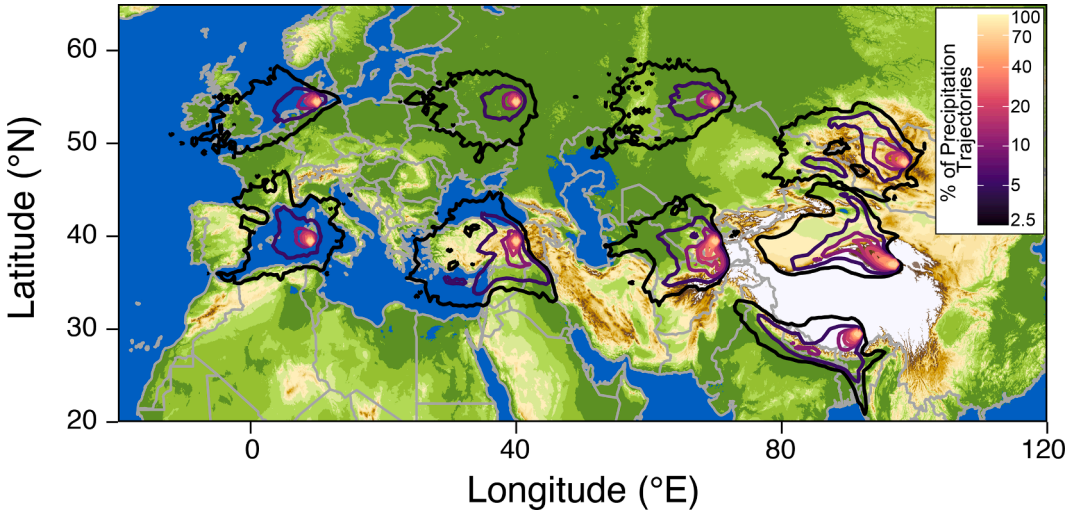

Fig. 2. Map of density contours of precipitation-producing air parcel back-trajectories at nine select locations in Eurasia for 2006–2016 simulated using HYSPLIT. Colored lines indicate contours of precipitation-producing trajectory density; dark lines indicate low density, while lighter tones indicate high density. Yellow diamonds indicate the starting point of each back-trajectory simulation. Note that the color scale for contour density is a log-scale.

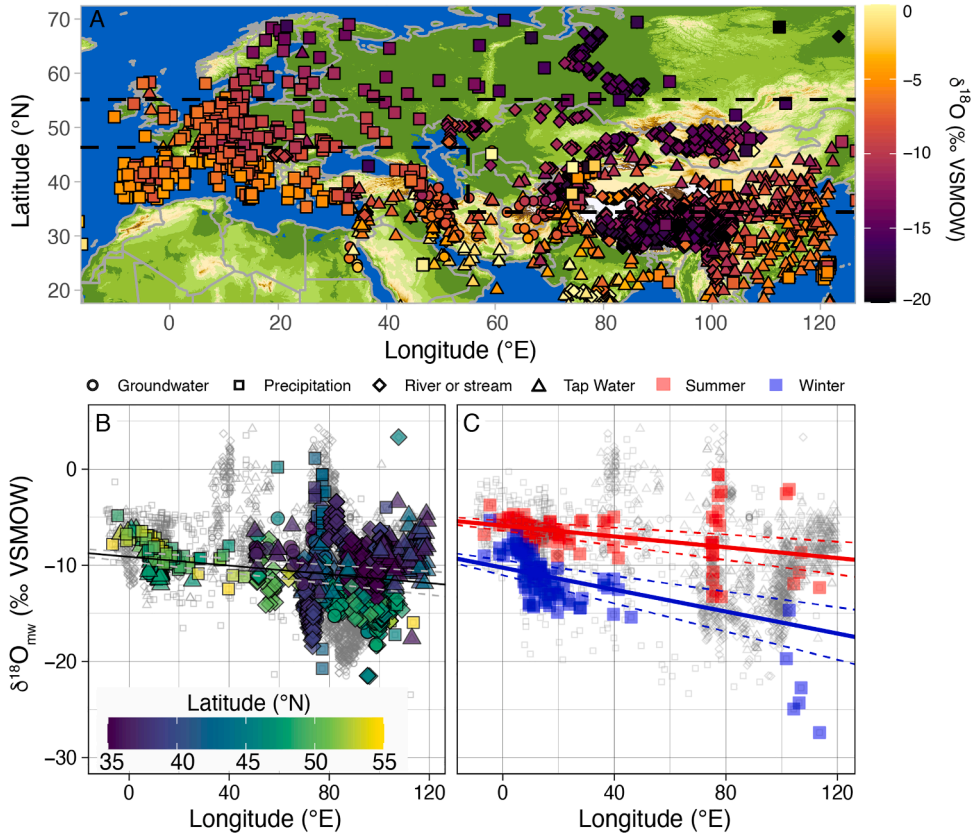

Fig. 3. A) Map of meteoric water $\delta^{18}O$ ($\delta^{18}O_{mw}$) from groundwater, precipitation (annual mean), river/stream water, and tap water (see Table S4). Data within dashed lines represent data falling within Atlantic-dominated moisture trajectories ("filtered data", 47°N-55°N in Europe, 35°N-55°N in Asia). B) Zonal gradient (black line) of modern $\delta^{18}O_{mw}$ (precipitation annual mean values are plotted), colored by latitude. Dashed lines represent the 95% confidence interval for the gradient. Colored and larger points represent "filtered data"; smaller, gray points are all points that fall outside of this range. C) Summer (JJA; red squares) and winter (DJF; blue squares) mean $\delta^{18}O_p$ values. Solid lines are regressions through the seasonal data and dashed lines are the 95% confidence interval. Gray points are all other meteoric water data (*i.e.*, groundwater, river/stream water, and tap water) from either JJA or DJF within the Atlantic-dominated moisture trajectory region ("filtered data" as before).

difference between two linear slopes (Cohen et al., 2003).

3.5. iCESM simulations

We perform two simulations using the isotope-enabled version of the Community Earth System Model (iCESM1.2; Brady et al. (2019)) at a nominal 2° horizontal resolution using prescribed pre-industrial phenology to directly simulate the impact of the atmospheric CO_2 concentrations on $\delta^{18}O_p$ in the absence of paleogeographic shifts or changes in land surface properties. The iCESM simulations explicitly model the fractionation of ^{16}O and ^{18}O in the atmosphere and land surface hydrologic cycle, including fractionation from evaporation on the land surface and condensation into clouds and precipitation. Both simulations were forced by prescribed sea surface temperatures and sea ice concentrations from two CESM2 simulations ("piControl" and "abrupt-4xCO2") included in the CMIP6 archive (Eyring et al., 2016). CO_2 mixing ratios for both the land and atmospheric models were held fixed at 284.7 or 1138.8 ppm for the piControl or 4xCO2 simulation, respectively. Both simulations were run for 15 years, with the first five years discarded to account for model spinup of surface temperature and the top 1 m of soil $\delta^{18}O$ (Fig. S5). When calculating transects of model parameters (Fig. 6), we use the same latitudinal bounds as for the data (see Section 3.3). Transects are calculated as the time mean of monthly mean model output for simulated years six through fifteen.

4. Results

4.1. HYSPLIT results

We find that the North Atlantic is the dominant moisture source for all latitudes (40°N-55°N) from 0°E until 10°E (Figs. 2, S1). East of 10°E, Atlantic moisture only dominates at and above approximately 45°N, whereas Mediterranean Sea moisture prevails for sites located between 40 and 45°N and between 10 and 40°E. The Black Sea, Baltic Sea, and Caspian Sea each influence nearby sites. Indian Ocean moisture is effectively blocked at latitudes > 35°N by the Tethyan ranges that bound Eurasia to the south. Eastward of 40°E and north of 35°N, westerly moisture dominates. Based on these HYSPLIT results and following previous work (Caves et al., 2015; Numaguti, 1999), we suggest that sites north of 47°N in Europe and north of 35°N in the interior of Asia receive dominantly westerly moisture (Figs. 2, S1).

4.2. Modern meteoric water $\delta^{18}O$

Generally, $\delta^{18}O_{mw}$ values are high in western Europe and progressively decrease across interior Eurasia (Fig. 3) (Rozanski et al., 1993). The lowest values in all of Eurasia are observed in the Himalayas, which receive moisture that is highly distilled due to orographic forcing of South Asian Monsoon rainfall (Araguás-Araguás et al., 1998; Wang et al., 2017). The high latitudes (> 55°N) also have low $\delta^{18}O_{mw}$ due to distillation of moisture during poleward moisture transport (Winnick et al., 2015). There are prominent examples of regional minima in $\delta^{18}O_p$

in interior Eurasia as well. The windward flanks of the ranges in interior Asia, such as the Tien Shan, Altai, and Hangay, have low $\delta^{18}O_{mw}$, which has been attributed to a combination of orographic rainout and precipitation seasonality, which is focused predominantly in the spring and fall (Fig. 1) (Caves et al., 2017; Rugenstein et al., 2022). Around the Mediterranean, particularly to the east, $\delta^{18}O_{mw}$ is higher than across much of central and northern Europe. In east Asia (*i.e.*, > 110° E), $\delta^{18}O_{mw}$ is relatively high due to the mixture of East Asian Monsoon moisture with westerly moisture (Araguás-Araguás et al., 1998). When plotted against longitude (Fig. 3B), the best-fit linear regression shows a decrease in $\delta^{18}O_{mw}$ eastward (slope = −0.023‰/°E). The scatter in the $\delta^{18}O_{mw}$ data also increases eastward, largely due to inclusion of data from the high-elevation Tian Shan and Mongolian Plateau (Caves et al., 2015). When only examining $\delta^{18}O_p$ (Fig. 3C), the JJA zonal $\delta^{18}O_p$ gradient is shallower than the wintertime (DJF) zonal $\delta^{18}O_p$ gradient. This trend of decreasing or largely invariant $\delta^{18}O$ eastward holds across different types of water (*i.e.*, precipitation, groundwater and river/-stream water, and tap water), with slopes ranging from −0.031 ‰/°E to 0.011 ‰/°E (Fig. S15). This trend also holds when excluding data from East Asia (*i.e.*, > 110° E) that might be impacted by air mass mixing (Fig. S15A; slope = −0.032 ‰/°E) or high-elevation data (*i.e.* > 1500 m) that may be impacted by orographic precipitation processes (Fig. S15B; slope = −0.009 ‰/°E).

4.3. Past precipitation $\delta^{18}O$

The spatial distribution of past $\delta^{18}O_p$ reconstructed from proxy $\delta^{18}O_{c/e}$ is similar to the modern, but with variations in the absolute value of past $\delta^{18}O_p$ between different geologic epochs (Fig. 4; Table 1). In nearly all epochs, past $\delta^{18}O_p$ values decrease towards the east, as observed in the modern. There are also similar regional trends throughout the Cenozoic, such as persistently low past $\delta^{18}O_p$ in southern Tibet. High, past $\delta^{18}O_p$ values around the Mediterranean persist throughout the Miocene. Average past $\delta^{18}O_p$ values for interior Asia (>50°E, 35–55°N) remain relatively invariant throughout the Cenozoic

Table 1
Means and 1σ of reconstructed past $\delta^{18}O_p$ in Europe and Asia of filtered data (<50°E: 47°–55°N; >50°E: 35°–55°N), organized by epoch (the Miocene is split into the early and late Miocene due to the abundance of Miocene data). The P-value is derived from a *t*-test of significant difference between the Asia and Europe populations within a single epoch. All values given in VSMOW (‰) (past zonal $\delta^{18}O_p$ gradient: ‰/°longitude). See Tables S1 and S2 for *t*-tests between epochs of Asia and Europe sample populations and Figure S11 for box plots of the Europe and Asia past $\delta^{18}O_p$ in different epochs.

Geologic Epoch	Europe $\delta^{18}O_p$	1σ	Asia $\delta^{18}O_p$	1σ	p-value	Gradient
Modern	−9.06	1.61	−11.15	3.20	2.24e-26*	−0.023
Quaternary	−8.84	2.53	−8.89	2.21	0.093	−0.0075
Pliocene	−9.30	0.98	−8.41	1.82	0.075	0.012
Late Miocene	−2.47	3.44	−7.49	1.77	0.0021*	−0.062
Early Miocene	−3.38	3.75	−8.95	1.83	5.00e-04*	−0.065
Oligocene	−3.06	3.93	−9.31	1.91	4.69e-06*	−0.076
Eocene	−2.74	3.21	−7.58	1.80	8.95e-07*	−0.058

* Indicates significant difference between Europe and Asia isotope populations ($p < 0.05$).

(Table S1; Fig. S11), with mean values of the filtered data varying only by ~2‰, between −9.31 ± 1.91‰ (Oligocene; $n = 30$ sites) and −7.49 ± 1.77‰ (late Miocene; $n = 26$ sites). Conversely, there is a pronounced decrease in past $\delta^{18}O_p$ in Europe between the late Miocene (−2.47 ± 3.44‰; $n = 9$ sites) and Pliocene (−9.30 ± 0.98‰; $n = 8$ sites). From the Eocene through the late Miocene, past $\delta^{18}O_p$ in Europe is statistically indistinguishable and high; in the Pliocene and Quaternary, past $\delta^{18}O_p$ is statistically indistinguishable and low (Table S2; Fig. S11).

The slope of past zonal $\delta^{18}O_p$ gradients varies through time. The zonal $\delta^{18}O_p$ gradient is shallowest in the Quaternary and Pliocene, with no statistical difference between Europe and interior Asia past $\delta^{18}O_p$ in these epochs or between the zonal slopes (Fig. 5; Tables 1, 2; Fig. S11).

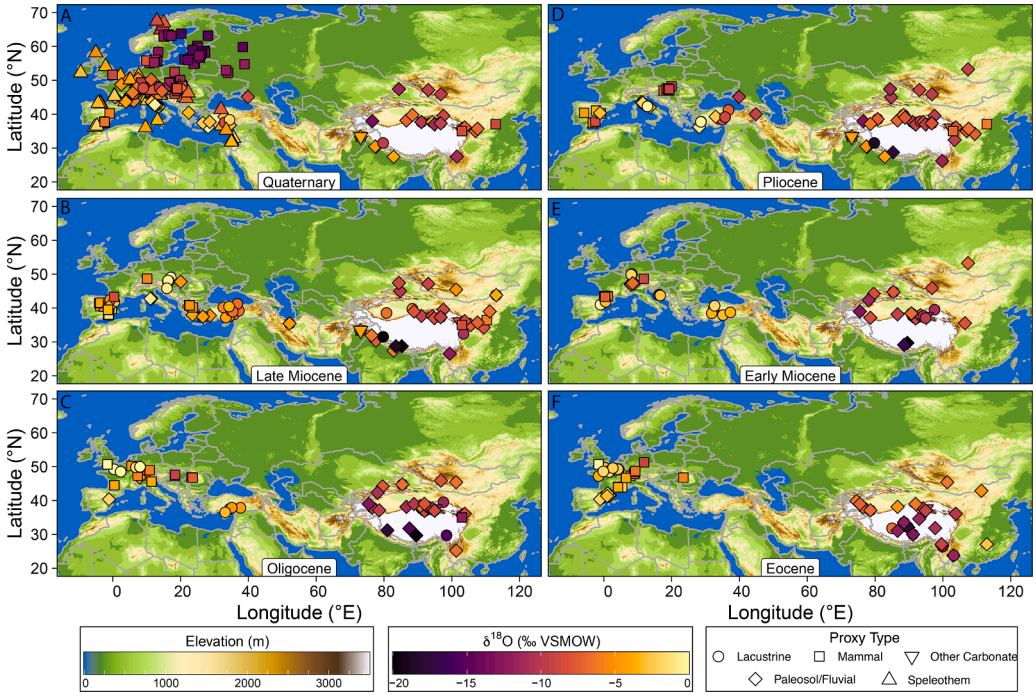

Fig. 4. Maps of past $\delta^{18}O_p$ reconstructed from proxy $\delta^{18}O_{c/e}$ for the Quaternary through the Eocene. Values of past $\delta^{18}O_p$ are reconstructed from $\delta^{18}O_c$ using interpolated summer (JJA) 2 m surface air temperatures (Kanamitsu et al., 2002), adjusted for estimated global paleotemperatures at time of mineral formation (Lear et al., 2000), and equilibrium fractionation factors (Kim and O'Neil, 1997). Values of past $\delta^{18}O_p$ are reconstructed from $\delta^{18}O_e$ using either mammal-specific or general (Amiot et al., 2004; Zanazzi et al., 2007) equations. (A) Quaternary. (B) Pliocene. (C) Late Miocene. (D) Early Miocene. (E) Oligocene. (F) Eocene.

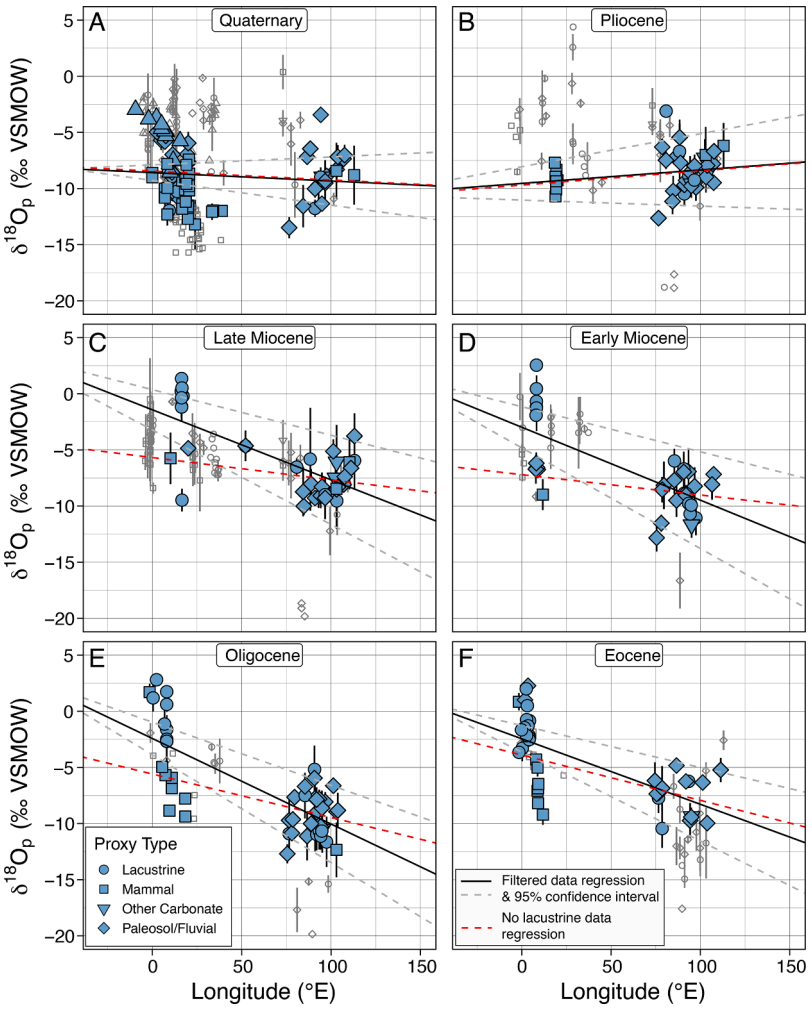

Fig. 5. Zonal $\delta^{18}O_p$ gradients (black lines) reconstructed from proxy $\delta^{18}O_{c/e}$ for the Quaternary through the Eocene using average summer (JJA) 2 m surface air temperature. Gray dashed lines indicate the 95% confidence interval for the reconstructed gradients. Red dashed lines show the zonal $\delta^{18}O_p$ gradient without lacustrine $\delta^{18}O_c$ data. Colored and larger points represent data falling within Atlantic-dominated moisture trajectories ("filtered data; 47°N-55°N in Europe, 35°N-55°N in Asia); smaller, gray points are all points that fall outside of this range. A: Quaternary; B: Pliocene; C: Late Miocene; D: Early Miocene; E: Oligocene; F: Eocene.

The zonal gradients are steepest in earlier epochs, with the highest gradients in the late Miocene, early Miocene, Oligocene, and Eocene. Each of these four periods have statistically distinct past $\delta^{18}O_p$ between Europe and interior Asia, but the zonal gradients between these time periods are not statistically different (Tables 1, 2; Fig. S11). The only statistically distinct change in the zonal gradient occurs between the late Miocene and Pliocene (Table 2). These shifts do not appear to be caused by large differences in past $\delta^{18}O_p$ due to different proxy types, as there is substantial overlap in past $\delta^{18}O_p$ among all proxy types (Figs. S9-S10). Though we plot this in Figs. 4 and 5 with modern latitude and longitude, calculating past zonal $\delta^{18}O_p$ gradients using paleo-coordinates due to plate movement during the Cenozoic (Seton et al., 2012) does not alter the trends presented above (Figs. S7-S8). Similarly, using mean annual or spatially constant surface air temperatures to reconstruct past $\delta^{18}O_p$ does not alter these trends (Figs. S12-S14).

4.4. *iCESM results*

Fig. 6 shows latitudinally averaged transects of $\delta^{18}O_p$, precipitable water, P, P-ET, and P/ET from the iCESM simulations taken across the length of interior Eurasia. Figs. 6A and 6B illustrate that the iCESM simulations successfully simulate a zonal $\delta^{18}O_p$ gradient and that this gradient becomes shallower in the $4xCO_2$ simulation. Precipitable water is approximately twice as high in the 4xCO2 simulation as it is in the piControl simulation, and the zonal decrease in precipitable water in the 4xCO2 simulation is smaller than the zonal decrease in precipitable water in the piControl simulation. In contrast, precipitation, evaporation, and runoff (*i.e.*, P minus E) show small or negligible changes between the two simulations.

5. Discussion

Our $\delta^{18}O$ compilation demonstrates a significant shallowing of past zonal $\delta^{18}O_p$ gradients across the continental interior of Eurasia over the Cenozoic and, importantly, differs from the change predicted by isotope-enabled climate model simulations. We suggest that the steeper zonal $\delta^{18}O_p$ gradients during past warm epochs indicates that net rainout was greater in higher CO_2 climates than today. However, there are several factors that can decouple $\delta^{18}O_{c/e}$ from past $\delta^{18}O_p$, such as diagenesis or evaporation. Further, changes in paleogeography, including changing inland sea or ice sheet extent, complicate direct comparison between our reconstructed zonal $\delta^{18}O_p$ gradients and the simulated $\delta^{18}O_p$ gradients. We first discuss and compare the simulated and reconstructed zonal $\delta^{18}O_p$ gradients, and then we examine several factors which might explain the divergent simulated and reconstructed zonal $\delta^{18}O$ gradients.

Table 2
Significance of differences in the reconstructed zonal $\delta^{18}O_p$ gradients using the filtered data (<50°E: 47°−55°N; >50°E: 35°−55°N). Difference significance is measured between time-adjacent epochs using 1) confidence intervals at which the slope of the zonal $\delta^{18}O_p$ gradients are statistically distinct and 2) p-values from *t*-test of significant difference between gradients between epochs (Cohen et al., 2003). The only statistically significant difference in the reconstructed zonal $\delta^{18}O_p$ gradients occurs between the Pliocene and late Miocene.

Geologic Epoch	Confidence Interval at which Slopes are different (with lacustrine data)	P-value	Confidence Interval at which Slopes are different (without lacustrine data)	P-value
Modern-Quaternary	99%	0.053	93%	0.076
Quaternary-Pliocene	99%	0.087	98%	0.065
Pliocene-late Miocene	99%	0.0005 *	99%	0.048 *
late Miocene-early Miocene	18%	0.87	9%	0.93
early Miocene-Oligocene	63%	0.47	90%	0.22
Oligocene-Eocene	92%	0.26	10%	0.93

* Indicates statistically significant change in the isotope gradient between epochs ($p < 0.05$).

5.1. Simulated zonal $\delta^{18}O_p$ gradients

Zonal $\delta^{18}O_p$ gradients shallow as CO_2 rises in our iCESM experiments. We attribute this model behavior to the thermodynamic response of atmospheric moisture to warming (Held and Soden, 2006). Precipitable water increases at a faster rate than P and ET in response to warming, which results in a larger atmospheric moisture reservoir and, consequently, smaller changes in $\delta^{18}O_p$ spatially (van Dijk et al., 2020; Winnick et al., 2015). Though this thermodynamic explanation is only strictly applicable at the global scale, it does appear to also explain our modeled mid-latitude data, and previous work has found that this conceptual scaling of the hydrological cycle—that precipitable water increases faster than P—is valid almost everywhere (Siler et al., 2018).

Given that these thermodynamic mechanisms are well-understood and occur on a global basis even in the geologic past (van Dijk et al., 2020; Winnick et al., 2015), we view a shallowing of the zonal $\delta^{18}O_p$ gradient as the expectation for the data and any deviations from this signal must be due to other processes that modify either $\delta^{18}O_p$ or $\delta^{18}O_{c/e}$. Thus, we next seek to understand why our geological data disagrees with these iCESM results. That our reconstructed zonal $\delta^{18}O_p$ gradients steepen during epochs with high CO_2 suggests other processes either decouple the proxy $\delta^{18}O$ values from prevailing hydroclimate or that there are processes not captured in our iCESM simulations, such as different ice sheet extent or vegetation or mis-parameterized land surface processes, that modify the response of $\delta^{18}O_p$ to CO_2 forcing in the geologic past.

5.2. Modern and reconstructed zonal $\delta^{18}O_p$ gradients

Today, modern $\delta^{18}O_{mw}$ decreases eastward (Fig. 3), consistent with

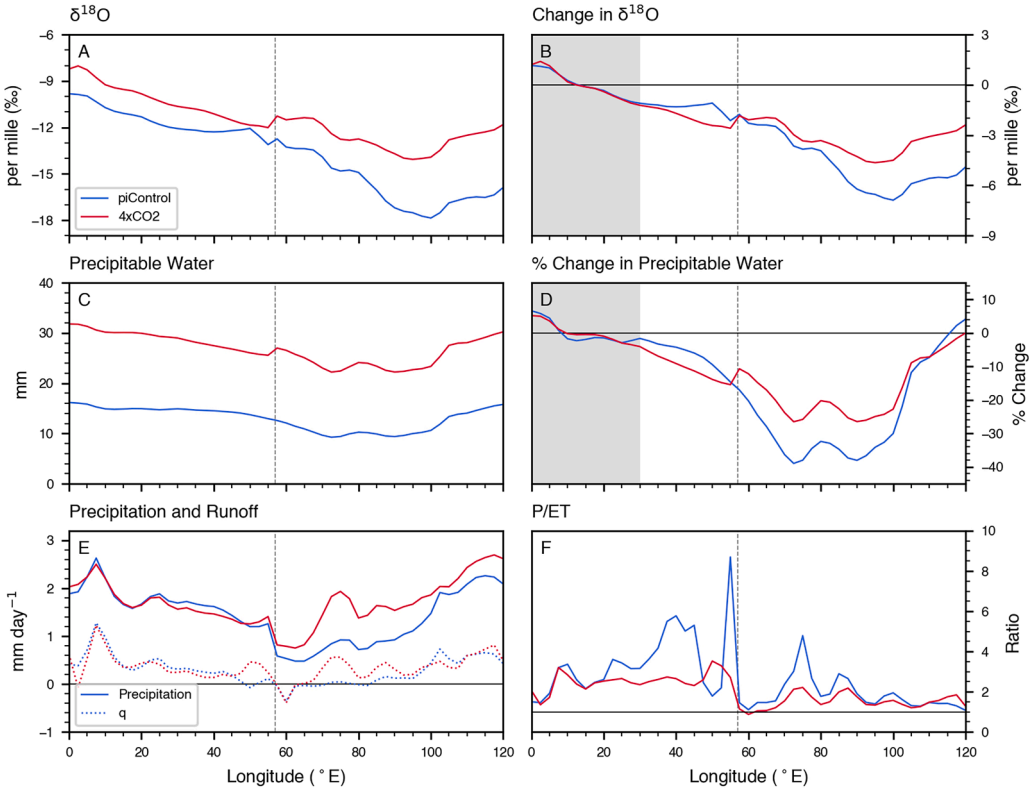

Fig. 6. Zonal profiles of iCESM output across Eurasia. Blue lines are from the piControl simulation (284.7 ppm CO_2); red lines are from the 4xCO_2 simulation (1138.4 ppm). A: $\delta^{18}O_p$ (‰); B: Change in $\delta^{18}O_p$ (‰) normalized to the $\delta^{18}O_p$ average between 0 and 30°E (shown in gray); C: Precipitable water (mm); D: Percentage change in precipitable water (%) normalized to the average precipitable water content between 0 and 30°E (shown in gray); E: Precipitation (P; solid lines) and runoff (q; dashed lines) (mm/day); F: P/ET. Thin dashed line at 57°E in all panels indicates the change in latitudinal width used to calculate these profiles (47°N-55°N in Europe, 35°N-55°N in Asia). Note that for the iCESM output, the change in latitudinal width occurs at 57°E and not at 50°E (as for the filtered data) to avoid averaging data over the Caspian Sea.

the idea that $\delta^{18}O_{mw}$ gradually decreases across continental interiors due to progressive rainout of moisture (Rozanski et al., 1993). Similarly, the JJA zonal $\delta^{18}O_p$ gradient is shallower than the DJF zonal $\delta^{18}O_p$ gradient (Fig. 3C), again consistent with the idea that ET during JJA re-supplies the westerlies with higher $\delta^{18}O$ moisture (Kurita et al., 2004). Though the precise slope of this zonal $\delta^{18}O_{mw}$ gradient is sensitive to the data included in the linear regression (Fig. S15), in all cases, the slope of the modern zonal $\delta^{18}O_{mw}$ gradient is shallower than the reconstructed zonal $\delta^{18}O_p$ gradients from the Eocene to the late Miocene. Indeed, if the range of slopes of the modern zonal $\delta^{18}O_{mw}$ gradient is taken as a measure of uncertainty as to the true slope, these values encompass the slope of the reconstructed Quaternary and Pliocene zonal $\delta^{18}O_p$ gradients.

Reconstructed zonal $\delta^{18}O_p$ gradients are steeper during high-CO_2 epochs, and the shift from steep to shallow gradients occurs between the late Miocene and Pliocene. Because mean past $\delta^{18}O_p$ in interior Asia has remained largely invariant over the Cenozoic (Tables 1, S1) (Caves et al., 2015), varying only by ~2‰ between the Eocene to the Quaternary, the shallowing of the zonal gradient between the late Miocene and Pliocene is caused by a decrease in mean past $\delta^{18}O_p$ in Europe, which decreases ~7‰ between the Miocene and Pliocene (Tables 1, S2). This $\delta^{18}O_p$ decrease may be attributable to the paucity of Pliocene data in Europe, which are all located in modern-day Hungary and Slovakia. These sites are thus relatively far inland compared with the spatial distribution of data in other epochs (Figs. 4, 5) and, consequently, these samples likely record already distilled moisture, typically reduced by several per mille relative to western Europe $\delta^{18}O_p$ (McDermott et al., 2011; Rozanski et al., 1993). Thus, these data may not record the initial zonal $\delta^{18}O_p$, but are rather lower due to their inland location, thereby artificially shallowing the zonal $\delta^{18}O_p$ gradient. Further, the only Pliocene samples are of the same proxy type (mammal tooth enamel), potentially further biasing our reconstructed zonal gradient. However, there is substantially more Quaternary data, including all proxy types, that cover a greater geographic distribution. Our reconstructed Quaternary zonal $\delta^{18}O_{pp}$ gradient is statistically indistinguishable from the Pliocene zonal gradient and similar to the modern $\delta^{18}O$ gradient, suggesting that a shallow, late Cenozoic zonal $\delta^{18}O_p$ gradient is a robust feature of the data. Thus, while we cannot confidently state that the shallowing of the longitudinal profile occurred at the Miocene-Pliocene boundary, it certainly had occurred by the Quaternary.

5.3. Parsing model-data disagreement

There are several factors that may explain the divergent responses of the data and modeled zonal $\delta^{18}O_p$ gradients to varying CO_2. Such factors include mechanisms that could decouple $\delta^{18}O_{c/e}$ from hydroclimate changes, shifts in paleogeography that alter $\delta^{18}O_p$, but are not accounted for in our iCESM simulations, and/or mis-representations of land surface or isotope fractionation processes in iCESM. Below, we discuss these processes and conclude with the most likely reasons that our reconstructed and simulated zonal $\delta^{18}O_p$ gradients diverge.

5.3.1. Mechanisms to decouple proxy $\delta^{18}O$ from hydroclimate changes

Several factors can modify $\delta^{18}O_{c/e}$ independent of the original past $\delta^{18}O_p$. Burial diagenesis induces a temperature-dependent fractionation that tends to lower the $\delta^{18}O$ preserved in minerals due to high burial temperatures (Garzione et al., 2004). However, Paleogene $\delta^{18}O_c$ data from Europe, which given its age may have experienced some degree of burial diagenesis, has instead higher $\delta^{18}O_c$ values than late Cenozoic $\delta^{18}O_c$ data. We note there are only small changes in the interior Asia $\delta^{18}O_c$ data. Thus, we suggest that diagenesis is not the cause of past steeper zonal $\delta^{18}O_p$ gradients.

Evaporation frequently affects lacustrine carbonates by increasing lake water ^{18}O, thus increasing $\delta^{18}O_c$ above $\delta^{18}O_p$; however, while evaporation affects the exact slope of the reconstructed zonal $\delta^{18}O_p$ gradients (Fig. 5), we suggest that evaporation is not the primary reason why these gradients are steeper under higher CO_2. Though the data from Asia have been previously screened for evaporative effects (Rugenstein and Chamberlain, 2018), we screened the Europe data for evaporative effects by using only the lowest 20% of $\delta^{18}O_c$ values (black lines in Fig. 5) (Li et al., 2015). However, even when all lacustrine data are removed from the analyses, we still find the same general trend of shallower zonal $\delta^{18}O_p$ gradients in the late Cenozoic (red dashed lines in Fig. 5). Additionally, although the gradients with no lacustrine data are shallower in the Eocene, Oligocene, and Miocene relative to the gradients with lacustrine data, we observe that both with and without lacustrine samples, the only occurrence of a statistically significant change in the slope of the zonal $\delta^{18}O_p$ profile is between the late Miocene and Pliocene (Table 2), suggesting that the results are robust even after removing those samples most likely affected by evaporation. Finally, in both the Eocene and Oligocene, there are non-lacustrine proxy data in Europe with similarly high $\delta^{18}O_c$ values, suggesting high $\delta^{18}O_c$ in the early Cenozoic in Europe is not merely an evaporative effect.

5.3.2. Paleogeographic and paleoclimatic changes

Major changes in paleogeography have occurred in Eurasia during the Cenozoic, potentially impacting moisture sources and the seasonality of precipitation. Importantly, these paleogeographic changes are not accounted for in our iCESM simulations. Paleogeographic changes include topographic changes associated with closure of the Tethys Ocean and related uplift of Tethyan ranges stretching from the Pyrenees to the Himalayas (Botsyun et al., 2019; Campani et al., 2012; Huyghe et al., 2012); continued westward retreat and shrinkage of the Paratethys during the Neogene (Popov et al., 2006), and; northern high latitude glaciation and vegetation changes, which became particularly pronounced in the Quaternary as boreal forests were replaced by tundra (Feng et al., 2022; Mudelsee and Raymo, 2005).

Each of these paleogeographic changes would result in predictable changes in $\delta^{18}O_p$ across Eurasia. The Tethyan ranges predominantly block southerly (*e.g.*, Mediterranean Sea or Indian Ocean) moisture from reaching northern Eurasia given their orientation, rather than blocking Atlantic or continental westerly moisture (Rugenstein and Chamberlain, 2018) (Figs. 1,2). Previous work suggests that this blocking of southerly moisture has been a long-standing feature in Eurasia, supported by low $\delta^{18}O$ directly in the lee of the Himalayas (Fig. 4) and high $\delta^{18}O$ in interior Asia throughout the Cenozoic (Caves et al., 2015; Rugenstein and Chamberlain, 2018). Further, the timing of uplift of these Tethyan ranges is not coincident with changes in the zonal $\delta^{18}O_p$ gradient. In particular, if these ranges did not block moisture at some point in the past and monsoonal moisture—transported for example by a northward shifted East African low-level jet—reached farther north, this would result in high $\delta^{18}O$ moisture being transported into interior Eurasia; however, in the Paleogene, interior Asia $\delta^{18}O_p$ is similar to and somewhat lower than Neogene $\delta^{18}O_p$ (Caves et al., 2015). In Europe, past $\delta^{18}O_p$ does decrease as perhaps expected due to distillation of moisture over high topography, but this $\delta^{18}O_p$ decrease does not correspond temporally with uplift of any of the major ranges in Europe that block Mediterranean moisture (Campani et al., 2012; Huyghe et al., 2012; San Jose et al., 2020). Thus, we suggest that the uplift of these Tethyan ranges—and hence changes in the blocking of southerly moisture—in Eurasia does not explain why reconstructed zonal $\delta^{18}O_p$ gradients were steeper in the geologic past.

If the Tethys and Paratethys provided a substantial moisture source in the middle of Eurasia, we would expect past $\delta^{18}O_p$ in interior Asia to be substantially higher, given that these marginal seas had $\delta^{18}O$ values near 0‰ and would therefore be supplying relatively high $\delta^{18}O$ moisture downwind, relative to continental-derived moisture $\delta^{18}O$ (<< 0‰). Yet, past $\delta^{18}O_p$ in interior Asia is not higher in the Paleogene and is, indeed, substantially lower than past $\delta^{18}O_p$ values in Europe. Thus, while the expected effect of the Tethys and Paratethys on zonal $\delta^{18}O_p$ gradients would be to shallow these gradients, we instead observe that the steepest

zonal gradients coincide with peak spatial extent of these inland seas.

Lastly, Northern Hemisphere glaciation and vegetation change is thought to have had major effects on atmospheric circulation (Feng et al., 2022); the midlatitude westerlies were likely weaker and shifted poleward during the warmer early Pliocene, then stronger and shifted equatorward after Northern Hemisphere glaciation ~2.7 Ma (Abell et al., 2021). The timing of the $\delta^{18}O_p$ decrease in Europe in the Pliocene and Quaternary approximately coincides with these changes. The combined effect of glaciation and high latitude vegetation change is thought to modify the position and strength of Northern Hemisphere stationary waves and the high latitude latent heat flux, both of which will modify moisture transport across Eurasia (Feng et al., 2022). South-shifted and strengthened westerlies may have contributed to lower $\delta^{18}O_p$ in Europe by displacing any southerly derived moisture with lower, North Atlantic-derived $\delta^{18}O$ westerly moisture (*i.e.*, Gao et al., 2021). Further, interactions between ice sheet growth and North Atlantic circulation may have also changed precipitation seasonality (Methner et al., 2020), shifting precipitation towards the shoulder seasons and dampening precipitation derived from summertime convective activity (McDermott et al., 2011) due to the southward shift of the mid-latitude westerlies. Some authigenic mineral proxies—such as paleosol carbonates—are particularly sensitive to precipitation seasonality and tend to reflect the $\delta^{18}O_p$ value from the rainy season (Breecker et al., 2009; Caves et al., 2017). Such seasonality changes may have imparted a significant effect on $\delta^{18}O_{c/e}$ because $\delta^{18}O_p$ seasonal variability is high across Eurasia (Fig. 3C) (Araguás-Araguás et al., 1998; Rozanski et al., 1993). Variable precipitation seasonality may explain why past $\delta^{18}O_p$ in Europe declined, but there was no corresponding shift in past $\delta^{18}O_p$ in interior Asia, as precipitation seasonality in interior Asia is thought to be dominantly controlled by topography rather than the presence of Northern Hemisphere ice (Rugenstein et al., 2022; Rugenstein and Chamberlain, 2018). The net effect of all these factors may have substantially decreased past $\delta^{18}O_p$ in Europe, and the timing of this decrease suggests it may have been influenced by Northern Hemisphere glaciation and high-latitude vegetation changes. Because ice sheet extent and vegetation in our iCESM simulations remain fixed, this effect on Eurasia hydroclimate is not captured in our simulations and may explain the divergent responses at high CO_2 in the zonal $\delta^{18}O_p$ gradient.

5.3.3. *Absent or poorly constrained land surface processes in iCESM*

The fact that reconstructed zonal $\delta^{18}O_p$ gradients steepen rather than shallow suggests that other processes that affect net rainout and runoff generation—besides the thermodynamic response of the hydrological cycle to warming—may exert a substantial effect on the terrestrial hydrological cycle in response to warming. How these processes, many encapsulated within the land surface model, will change in response to warming remain uncertain (Fisher et al., 2019). Our simulations suggest that these absent or largely parameterized processes result in a shallowing of the zonal $\delta^{18}O_p$ gradient rather than the observed steepening.

Though a full accounting of the effect of these parameters on $\delta^{18}O$ is outside the scope of this study, we focus here on three processes that control ET and q and which are thought to change in a warmer world. These processes include *(1)* greater partitioning of annual precipitation into wet seasons and extreme storms, which will tend to produce greater q and reduced ET as plants are unable to use all of the available P during the wet season or during storms (Scheff et al., 2022); *(2)* plant physiological responses to rising CO_2, which are absent in our simulations and which can act to both reduce stomatal conductance (reducing transpiration) and/or spur increases in leaf area due to CO_2 fertilization (increasing transpiration) (Lemordant et al., 2018), and; *(3)* increases in the vapor pressure deficit due to rising temperatures that drive increased leaf-level evaporation (increasing transpiration) (Scheff et al., 2022). In models, many of these processes are emergent properties, partially controlled by many different land surface parameters, such as the Medlyn slope, specific leaf area, and soil properties (Fisher et al., 2019), whose sum in response to warming and rising CO_2 determine how these processes modify ET and q in warmer climates. Together, the sum of these, plus additional, processes determine whether P will be increasingly partitioned to q or to ET as CO_2 rises, thereby determining whether the ratio of P to ET will increase or decrease.

Models tend to show that, as CO_2 increases, q will increase at a slightly higher rate than P, suggesting that the fraction of P partitioned into ET will decrease slightly (Swann et al., 2016; Zhang et al., 2014). This increases the P/ET ratio and should result in a steepening of the zonal $\delta^{18}O_p$ gradient. However, higher precipitable water typically overwhelms this effect, resulting instead in shallower $\delta^{18}O_p$ gradients under high CO_2 in model simulations (see Fig. 6 and Section 5.1). Though our analysis cannot pinpoint which of the above processes may lead to the disagreement between the data and our simulations, the observed steeper zonal $\delta^{18}O_p$ gradients potentially indicate that a far greater fraction of P should be partitioned to q in a higher CO_2 world, thereby resulting in a steeper zonal $\delta^{18}O_p$ gradient despite the effect of increasing precipitable water. Our simulations, in contrast, show only a small or negligible increase in q across the continental interior of Eurasia (Fig. S16). Because the many parameters that control the partitioning of P on the land surface are difficult to empirically constrain (Fisher et al., 2019), small changes in these parameters (and in processes not included in our iCESM simulations) may modify the partitioning of P into ET and q. The implication of steeper reconstructed zonal $\delta^{18}O_p$ gradients than simulated by iCESM is thus that q may be much more sensitive to warming than P (and more sensitive than iCESM indicates (see Figure S16)), resulting in a substantial increase in the P/ET ratio in the mid-latitudes.

Additional factors that may decouple simulated and reconstructed zonal $\delta^{18}O_p$ gradients are incorrect parameterizations of the water cycle and associated isotopic fractionations during formation and evaporation of precipitation (Man et al., 2022). For example, isotope-enabled climate models struggle to properly simulate the observed relationship between convective precipitation fraction and $\delta^{18}O_p$ (Hu et al., 2018), and this fraction impacts interannual $\delta^{18}O_p$ (Aggarwal et al., 2016). The sum of these processes with warming will determine how simulated $\delta^{18}O_p$ changes across interior Eurasia, and any biases or mis-parameterizations may result in divergent simulated and observed zonal $\delta^{18}O_p$ gradients. Ultimately, further work to constrain why interior Asia $\delta^{18}O_p$ increases faster than $\delta^{18}O_p$ in western Eurasia as CO_2 rises in iCESM is necessary to understand this data-model disagreement.

6. Implications and conclusions

Our compilation of nearly 15,000 stable isotope samples from authigenic carbonates and tooth enamel from Eurasia over the Cenozoic demonstrates that past zonal $\delta^{18}O_p$ gradients have varied substantially, with steeper gradients during warmer, higher CO_2 epochs. Comparison of $\delta^{18}O_{c/e}$ data from Europe and Asia indicates that the shallower late Cenozoic zonal $\delta^{18}O_p$ gradient is driven primarily by a large decrease in $\delta^{18}O_{c/e}$ after the Miocene. Intriguingly, simulations using an isotope-enabled climate model (iCESM) indicate that, at higher CO_2, zonal $\delta^{18}O_p$ gradients shallow, in contrast to the observations. This data-model disagreement does not appear to be caused by diagenetic or evaporative effects, particularly as the same significant change in reconstructed zonal $\delta^{18}O_p$ gradients appears even when removing all lacustrine data. Further, despite substantial changes in the extent of inland seas and topography during the Cenozoic in Eurasia, changes in the reconstructed zonal $\delta^{18}O_p$ gradients do not appear to be driven by these paleogeographic changes.

Instead, we suggest that the divergent reconstructed and simulated $\delta^{18}O_p$ zonal gradients are due either to the effect of Northern Hemisphere ice sheet and vegetation changes on westerly moisture transport and precipitation seasonality or due to the absence or misrepresentation of land surface processes in iCESM that partition too much precipitation to ET in warmer, higher CO_2 climates. The timing of the shallowing of the zonal $\delta^{18}O$ gradient between the late Miocene and

Quaternary is approximately coincident with the inception and intensification of Northern Hemisphere ice growth and retreat of the boreal forest to the south. Thus, the divergent reconstructed and simulated zonal gradients may point to a fundamental control by ice sheets and high-latitude vegetation on Eurasia hydroclimate (Feng et al., 2022). Alternatively, many of the land-surface parameters in iCESM that collectively determine how P is partitioned to ET and q are poorly constrained, particularly as atmospheric CO_2 and temperature increases (Fisher et al., 2019). Thus, the divergent reconstructed and zonal gradients may arise due to prescribed rather than interactive phenology and parameterizations in iCESM that result in a greater fraction of P being partitioned to ET, lowering the P/ET ratio, and shallowing the zonal $\delta^{18}O_p$ gradient. Because the effect of rising precipitable water on $\delta^{18}O$ gradients is well-established (van Dijk et al., 2020; Winnick et al., 2015), if these land surface processes are responsible for the data-model disagreement, then the steeper reconstructed zonal $\delta^{18}O_p$ gradients indicate that q must be substantially more sensitive to rising CO_2 than currently estimated. Distinguishing between whether model boundary conditions, the prescribed phenology in our simulations, or mis-parameterizations in the land surface and isotope modules of iCESM drives this data-model disagreement will require additional work, including isotope-enabled model simulations with interactive phenology, different ice sheet and land surface boundary conditions, and further data from the late Cenozoic and from additional sites and proxy sites that are poorly represented.

Ultimately, our ability to understand the response of the critical parameters of P, ET, and q to warming is partly limited by our inability to constrain how the land surface—and its role in the water cycle—will respond to warming. This uncertainty makes the geologic record of $\delta^{18}O$ particularly promising as a way of probing how the terrestrial water cycle responds to warming. Based upon this premise, we tested model projections of warming against geologic data that potentially isolates the role of the land surface in the terrestrial hydrological cycle and found a substantial data-model disagreement. Parsing the reasoning behind the model-data discrepancy found herein will ultimately yield greater confidence in models and in our understanding of the evolution of past climates over Earth's largest continental landmass.

CRediT authorship contribution statement

Ellie Driscoll: Writing – review & editing, Writing – original draft, Methodology, Funding acquisition, Formal analysis, Conceptualization. **Michael R. Needham:** Writing – review & editing, Methodology, Funding acquisition, Formal analysis, Conceptualization. **Patrick W. Keys:** Writing – review & editing, Software. **Jeremy K.C. Rugenstein:** Writing – review & editing, Project administration, Methodology, Funding acquisition, Conceptualization.

Declaration of competing interest

The authors declare that they have no known competing financial interests or personal relationships that could have appeared to influence the work reported in this paper.

Data availability

The compiled data is available at the PATCH Lab and in Tables S3 and S4.

Acknowledgments

We thank the many individuals who provided valuable feedback on this project, including Tyler Kukla, Scott Denning, Mike Ronayne, members of the CSU GeoPAST group, and participants in ATS/GEOL 580A1 Paleoclimate. We also thank Tripti Bhattacharya and an anonymous reviewer for comments that substantially clarified the arguments presented herein. Driscoll was partially funded by a Warner Graduate Research Fellowship. An NCAR student small-grant allocation to Needham and Driscoll funded core hours to perform iCESM simulations on the Cheyenne supercomputer. This work was also funded by NSF EAR-2316733 to Rugenstein.

Supplementary materials

Supplementary material associated with this article can be found, in the online version, at doi:10.1016/j.epsl.2024.118623.

References

Abell, J.T., Winckler, G., Anderson, R.F., Herbert, T.D., 2021. Poleward and weakened westerlies during Pliocene warmth. Nature 589, 70–75. https://doi.org/10.1038/s41586-020-03062-1.

Aggarwal, P.K., Romatschke, U., Araguas-Araguas, L., Belachew, D., Longstaffe, F.J., Berg, P., Schumacher, C., Funk, A., 2016. Proportions of convective and stratiform precipitation revealed in water isotope ratios. Nat. Geosci. 9, 624–629. https://doi.org/10.1038/ngeo2739.

Aizen, E.M., Aizen, V.B., Melack, J.M., Nakamura, T., Ohta, T., 2001. Precipitation and atmospheric circulation patterns at mid-latitudes of Asia. Int. J. Climatol. 21, 535–556. https://doi.org/10.1002/joc.626.

Amiot, R., Lécuyer, C., Buffetaut, E., Fluteau, F., Legendre, S., Martineau, F., 2004. Latitudinal temperature gradient during the Cretaceous Upper Campanian-Middle Maastrichtian: $\delta^{18}O$ record of continental vertebrates. Earth Planet. Sci. Lett. 226, 255–272. https://doi.org/10.1016/j.epsl.2004.07.015.

Araguás-Araguás, L., Froehlich, K., Rozanski, K., 1998. Stable isotope composition of precipitation over southeast Asia. J. Geophys. Res. 103, 28721–28742.

Baldwin, J., Vecchi, G., 2016. Influence of the Tian Shan mountains on arid extratropical Asia. J. Clim. 29, 5741–5762. https://doi.org/10.1175/JCLI-D-15-0490.1.

Botsyun, S., Sepulchre, P., Donnadieu, Y., Risi, C., Licht, A., Caves Rugenstein, J.K., 2019. Revised paleoaltimetry data show low Tibetan Plateau elevation during the Eocene. Science 363, 946. https://doi.org/10.1126/SCIENCE.AAQ1436.

Brady, E., Stevenson, S., Bailey, D., Liu, Z., Noone, D., Nusbaumer, J., Otto-Bliesner, B.L., Tabor, C., Tomas, R., Wong, T., Zhang, J., Zhu, J., 2019. The connected isotopic water cycle in the community earth system model version 1. J. Adv. Model. Earth Syst. 11, 2547–2566. https://doi.org/10.1029/2019MS001663.

Breecker, D.O., Sharp, Z.D., McFadden, L.D., 2009. Seasonal bias in the formation and stable isotopic composition of pedogenic carbonate in modern soils from central New Mexico, USA. Geol. Soc. Am. Bull. 121, 630–640. https://doi.org/10.1130/B26413.1.

Campani, M., Mulch, A., Kempf, O., Schlunegger, F., Mancktelow, N., 2012. Miocene paleotopography of the Central Alps. Earth Planet. Sci. Lett. 337–338, 174–185. https://doi.org/10.1016/j.epsl.2012.05.017.

Caves, J.K., Bayshashov, B.U., Zhamangara, A., Ritch, A.J., Ibarra, D.E., Sjostrom, D.J., Mix, H.T., Winnick, M.J., Chamberlain, C.P., 2017. Late Miocene uplift of the Tian Shan and Altai and reorganization of Central Asia climate. GSA Today 27, 19–26. https://doi.org/10.1130/GSATG305A.1.

Caves, J.K., Winnick, M.J., Graham, S.A., Sjostrom, D.J., Mulch, A., Chamberlain, C.P., 2015. Role of the westerlies in Central Asia climate over the Cenozoic. Earth Planet. Sci. Lett. 428, 33–43. https://doi.org/10.1016/j.epsl.2015.07.023.

Cohen, J., Cohen, P., West, S.G., Aiken, L.S., 2003. Applied Multiple Regression/Correlation Analysis for the Behavioral Sciences. Lawrence Erlbaum Associates, Publishers, Mahwah, New Jersey, 3rd Editio.

Domingo, L., Koch, P.L., Hernández Fernández, M., Fox, D.L., Domingo, M.S., Alberdi, M. T., 2013. Late neogene and early quaternary paleoenvironmental and paleoclimatic conditions in southwestern europe: isotopic analyses on mammalian taxa. PLoS ONE 8. https://doi.org/10.1371/journal.pone.0063739.

Douville, H., Raghavan, K., Renwick, J., Allan, R.P., Arias, P.A., Barlow, M., Cerezo-Mota, R., Cherchi, A., Gan, T.Y., Gergis, J., Jiang, D., Khan, A., Pokam Mba, W., Rosenfeld, D., Tierney, J., Zolina, O., 2021. Water cycle changes. Masson-Delmotte, V., Zhai, P., Pirani, A., Connors, S.L., Péan, C., Berger, S., Caud, N., Chen, Y., Goldfarb, L., Gomis, M.I., Huang, M., Leitzell, K., Lonnoy, E., Matthews, J.B.R., Maycock, T.K., Waterfield, T., Yelekçi, O., Yu, R., Zhou, B. Climate Change 2021: The Physical Science Basis. Contribution of Working Group I to the Sixth Assessment Report of the Intergovernmental Panel on Climate Change. Cambridge University Press, p. 239.

Eyring, V., Bony, S., Meehl, G.A., Senior, C.A., Stevens, B., Stouffer, R.J., Taylor, K.E., 2016. Overview of the coupled model intercomparison project phase 6 (CMIP6) experimental design and organization. Geosci. Model Dev. 9, 1937–1958. https://doi.org/10.5194/gmd-9-1937-2016.

Feng, R., Bhattacharya, T., Otto-Bliesner, B.L., Brady, E.C., Haywood, A.M., Tindall, J.C., Hunter, S.J., Abe-Ouchi, A., Chan, W.-L., Kageyama, M., Contoux, C., Guo, C., Li, X., Lohmann, G., Stepanek, C., Tan, N., Zhang, Q., Zhang, Z., Han, Z., Williams, C.J.R., Lunt, D.J., Dowsett, H.J., Chandan, D., Peltier, W.R., 2022. Past terrestrial hydroclimate sensitivity controlled by Earth system feedbacks. Nat. Commun. 13, 1–11. https://doi.org/10.1038/s41467-022-28814-7.

Feng, R., Poulsen, C.J., Werner, M., Chamberlain, C.P., Mix, H.T., Mulch, A., 2013. Early Cenozoic evolution of topography, climate, and stable isotopes in precipitation in the

North American Cordillera. Am. J. Sci. 313, 613–648. https://doi.org/10.2475/07.2013.01.
Fisher, R.A., Wieder, W.R., Sanderson, B.M., Koven, C.D., Oleson, K.W., Xu, C., Fisher, J. B., Shi, M., Walker, A.P., Lawrence, D.M., 2019. Parametric Controls on Vegetation Responses to Biogeochemical Forcing in the CLM5. J. Adv. Model. Earth Syst. 11, 2879–2895. https://doi.org/10.1029/2019MS001609.
Gao, Yuan, Ibarra, D.E., Rugenstein, J.K.C., Kukla, T., Methner, K., Gao, Youfeng, Huang, H., Lin, Z., Zhang, L., Xi, D., Wu, H., Carroll, R., Graham, S.A., Chamberlain, C.P., 2021. Terrestrial climate in mid-latitude East Asia from the latest Cretaceous to the earliest Paleogene: a multiproxy record from the Songliao Basin in northeastern China. Earth-Science Rev 216, 103572. https://doi.org/10.1016/j.earscirev.2021.103572.
Garzione, C.N., Dettman, D.L., Horton, B.K., 2004. Carbonate oxygen isotope paleoaltimetry: evaluating the effect of diagenesis on paleoelevation estimates for the Tibetan plateau. Palaeogeogr. Palaeoclimatol. Palaeoecol. 212, 119–140. https://doi.org/10.1016/j.palaeo.2004.05.020.
Gat, J.R., Carmi, I., 1970. Evolution of the isotopic composition of atmospheric water in the Mediterranean Sea Area. J. Geophys. Res. 75, 3039–3048.
Held, I.M., Soden, B.J., 2006. Robust responses of the hydrological cycle to global warming. J. Clim. 19, 5686–5699.
Hu, J., Emile-Geay, J., Nusbaumer, J., Noone, D., 2018. Impact of convective activity on precipitation $\delta^{18}O$ in isotope-enabled general circulation models. J. Geophys. Res. Atmos. 123, 13595–13610. https://doi.org/10.1029/2018JD029187.
Huyghe, D., Mouthereau, F., Emmanuel, L., 2012. Oxygen isotopes of marine mollusc shells record Eocene elevation change in the Pyrenees. Earth Planet. Sci. Lett. 345–348, 131–141. https://doi.org/10.1016/j.epsl.2012.06.035.
IAEA/WMO, 2020a. Global Network of Isotopes in Rivers [WWW Document]. GNIR Database.
IAEA/WMO, 2020b. Global Network of Isotopes in Precipitation [WWW Document]. GNIP Database. URL. http://www.iaea.org/water. accessed 4.10.16.
Kanamitsu, M., Ebisuzaki, W., Woollen, J., Yang, S.-K., Hnilo, J.J., Fiorino, M., Potter, G. L., 2002. NCEP–DOE AMIP-II Reanalysis (R-2). Bull. Am. Meteorol. Soc. 83, 1631–1643. https://doi.org/10.1175/BAMS-83-11-1631.
Kim, S., O'Neil, J., 1997. Equilibrium and nonequilibrium oxygen isotope effects in synthetic carbonates. Geochim. Cosmochim. Acta 61, 3461–3475.
Koch, P., 2007. Isotopic study of the biology of modern and fossil vertebrates. In: Michener, R., Lajtha, K. (Eds.), Stable Isotopes in Ecology and Environmental Science: Second Edition2. Blackwell Publishing Ltd, Malden, MA, pp. 99–154.
Kohn, M.J., 1996. Predicting animal $\delta^{18}O$: accounting for diet and physiological adaptation. Geochim. Cosmochim. Acta 60, 4811–4829.
Kukla, T., Rugenstein, J.K.C., Driscoll, E., Ibarra, D.E., Chamberlain, C.P., 2022a. The PATCH Lab V1.0: a database and workspace for Cenozoic terrestrial paleoclimate and environment reconstruction. Am. J. Sci. 322, 1124–1158. https://doi.org/10.2475/10.2022.02.
Kukla, T., Rugenstein, J.K.C., Ibarra, D.E., Winnick, M.J., Strömberg, C.A.E., Chamberlain, C.P., 2022b. Drier winters drove Cenozoic open habitat expansion in North America. AGU Adv 3. https://doi.org/10.1029/2021AV000566 e2021AV000566.
Kukla, T., Winnick, M.J., Maher, K., Ibarra, D.E., Chamberlain, C.P., 2019. The sensitivity of terrestrial $\delta^{18}O$ gradients to hydroclimate evolution. J. Geophys. Res. Atmos. 124, 563–582. https://doi.org/10.1029/2018JD029571.
Kurita, N., Yoshida, N., Inoue, G., Chayanova, E.A., 2004. Modern isotope climatology of Russia: a first assessment. J. Geophys. Res. 109, D03102. https://doi.org/10.1029/2003JD003404.
Lear, C.H., Elderfield, H., Wilson, P.A., 2000. Cenozoic deep-sea temperatures and global ice volumes from Mg/Ca in benthic foraminiferal calcite. Science 287, 269–272. https://doi.org/10.1126/science.287.5451.269.
Lemordant, L., Gentine, P., Swann, A.S., Cook, B.I., Scheff, J., 2018. Critical impact of vegetation physiology on the continental hydrologic cycle in response to increasing CO_2. In: , 115. https://doi.org/10.1073/pnas.1720712115, 201720712.
Leng, M.J., Marshall, J.D., 2004. Palaeoclimate interpretation of stable isotope data from lake sediment archives. Quat. Sci. Rev. 23, 811–831. https://doi.org/10.1016/j.quascirev.2003.06.012.
Li, S., Currie, B.S., Rowley, D.B., Ingalls, M., 2015. Cenozoic paleoaltimetry of the SE margin of the Tibetan Plateau: constraints on the tectonic evolution of the region. Earth Planet. Sci. Lett. 1, 1–10. https://doi.org/10.1016/j.epsl.2015.09.044.
Liu, Z., Bowen, G.J., Welker, J.M., 2010. Atmospheric circulation is reflected in precipitation isotope gradients over the conterminous United States. J. Geophys. Res. 115, D22120. https://doi.org/10.1029/2010JD014175.
Man, W., Zhou, T., Jiang, J., Zuo, M., Hu, J., 2022. Moisture sources and climatic controls of precipitation stable isotopes over the tibetan plateau in water-tagging simulations. J. Geophys. Res. Atmos. 127, 1–15. https://doi.org/10.1029/2021JD036321.
Mankin, J.S., Seager, R., Smerdon, J.E., Cook, B.I., Williams, A.P., Horton, R.M., 2018. Blue water tradeoffs with vegetation in a CO_2-enriched climate. Geophys. Res. Lett. https://doi.org/10.1002/2018GL077051.
McDermott, F., Atkinson, T.C., Fairchild, I.J., Baldini, L.M., Mattey, D.P., 2011. A first evaluation of the spatial gradients in $\delta^{18}O$ recorded by European Holocene speleothems. Glob. Planet. Change 79, 275–287. https://doi.org/10.1016/j.gloplacha.2011.01.005.
Medlyn, B.E., Duursma, R.A., Eamus, D., Ellsworth, D.S., Prentice, I.C., Barton, C.V.M., Crous, K.Y., De Angelis, P., Freeman, M., Wingate, L., 2011. Reconciling the optimal and empirical approaches to modelling stomatal conductance. Glob. Chang. Biol. 17, 2134–2144. https://doi.org/10.1111/j.1365-2486.2010.02375.x.
Methner, K., Campani, M., Fiebig, J., Löffler, N., Kempf, O., Mulch, A., 2020. Middle Miocene long-term continental temperature change in and out of pace with marine climate records. Sci. Rep. 10, 1–10. https://doi.org/10.1038/s41598-020-64743-5.
Meyer-Christoffer, A., Becker, A., Finger, P., Rudolf, B., Schneider, U., Ziese, M., 2015. GPCC climatology version 2015 at 0.25°: monthly land-surface precipitation climatology for every month and the total year from rain-gauges built on GTS-based and historic data. https://doi.org/10.5676/DWD_GPCC/CLIM_M_V2015_025.
Mudelsee, M., Raymo, M.E., 2005. Slow dynamics of the Northern Hemisphere glaciation. Paleoceanography 20. https://doi.org/10.1029/2005PA001153.
Numaguti, A., 1999. Origin and recycling processes of precipitating water over the Eurasian continent: experiments using an atmospheric general circulation model. J. Geophys. Res. 104, 1957–1972.
Oshima, K., Tachibana, Y., Hiyama, T., 2015. Climate and year-to-year variability of atmospheric and terrestrial water cycles in the three great Siberian rivers. J. Geophys. Res. Atmos. 120, 3043–3062. https://doi.org/10.1038/175238c0.
Pendergrass, A.G., Hartmann, D.L., 2014. The atmospheric energy constraint on global-mean precipitation change. J. Clim. 27, 757–768. https://doi.org/10.1175/JCLI-D-13-00163.1.
Popov, S.V., Shcherba, I.G., Ilyina, L.B., Nevesskaya, L.a., Paramonova, N.P., Khondkarian, S.O., Magyar, I., 2006. Late Miocene to Pliocene palaeogeography of the Paratethys and its relation to the Mediterranean. Palaeogeogr. Palaeoclimatol. Palaeoecol. 238, 91–106. https://doi.org/10.1016/j.palaeo.2006.03.020.
Rozanski, K., Araguás-Araguás, L., Gonfiantini, R., 1993. Isotopic patterns in modern global precipitation. In: Swart, P.K., Lohmann, K.C., McKenzie, J.A., Savin, S.M. (Eds.), Climate Change in Continental Isotopic Records. Wiley Online Library, pp. 1–36.
Rugenstein, J.K.C., Chamberlain, C.P., 2018. The evolution of hydroclimate in Asia over the Cenozoic: a stable-isotope perspective. Earth-Sci. Rev. 185, 1129–1156. https://doi.org/10.1016/j.earscirev.2018.09.003.
Rugenstein, J.K.C., Methner, K., Kukla, T., Mulch, A., Lüdecke, T., Fiebig, J., Wegmann, K.W., Zeitler, P.K., Chamberlain, C.P., 2022. Clumped isotope constraints on warming and precipitation seasonality in Mongolia following Altai uplift. Am. J. Sci. 322, 28–54. https://doi.org/10.2475/01.2022.02.
San Jose, M., Caves Rugenstein, J.K., Cosentino, D., Faccenna, C., Fellin, M.G., Ghinassi, M., Martini, I., 2020. Stable isotope evidence for rapid uplift of the central Apennines since the late Pliocene. Earth Planet. Sci. Lett. 544, 116376 https://doi.org/10.1016/j.epsl.2020.116376.
Scheff, J., Coats, S., Laguë, M.M., 2022. Why do the global warming responses of land-surface models and climatic dryness metrics disagree? Earth's Futur. 10 https://doi.org/10.1029/2022EF002814.
Scheff, J., Seager, R., Liu, H., Coats, S., 2017. Are glacials dry? Consequences for paleoclimatology and for greenhouse warming. J. Clim. 30, 6593–6609. https://doi.org/10.1175/JCLI-D-16-0854.1.
Seton, M., Müller, R.D., Zahirovic, S., Gaina, C., Torsvik, T., Shephard, G., Talsma, A., Gurnis, M., Turner, M., Maus, S., Chandler, M., 2012. Global continental and ocean basin reconstructions since 200Ma. Earth-Sci. Rev. 113, 212–270. https://doi.org/10.1016/j.earscirev.2012.03.002.
Siler, N., Roe, G.H., Armour, K.C., 2018. Insights into the zonal-mean response of the hydrologic cycle to global warming from a diffusive energy balance model. J. Clim. https://doi.org/10.1175/JCLI-D-18-0081.1. JCLI-D-18-0081.1.
Stein, A.F., Draxler, R.R., Rolph, G.D., Stunder, B.J.B., Cohen, M.D., Ngan, F., 2015. NOAA's HYSPLIT atmospheric transport and dispersion modeling system. Bull. Am. Meteorol. Soc. 96, 2059–2077. https://doi.org/10.1175/BAMS-D-14-00110.1.
Swann, A.L.S., Hoffman, F.M., Koven, C.D., Randerson, J.T., 2016. Plant responses to increasing CO_2 reduce estimates of climate impacts on drought severity. Proc. Natl. Acad. Sci 113, 10019–10024. https://doi.org/10.1073/pnas.1604581113.
van der Ent, R.J., Savenije, H.H.G., Schaefli, B., Steele-Dunne, S.C., 2010. Origin and fate of atmospheric moisture over continents. Water Resour. Res. 46 https://doi.org/10.1029/2010WR009127.
van Dijk, J., Fernandez, A., Bernasconi, S.M., Rugenstein, J.K.C., Passey, S.R., White, T., 2020. Spatial pattern of super-greenhouse warmth controlled by elevated specific humidity. Nat. Geosci. 13, 739–744. https://doi.org/10.1038/s41561-020-00648-2.
Wang, S., Zhang, M., Crawford, J., Hughes, C.E., Du, M., Liu, X., 2017. The effect of moisture source and synoptic conditions on precipitation isotopes in arid central Asia. J. Geophys. Res. Atmos. 122, 2667–2682. https://doi.org/10.1002/2015JD024626.
Winnick, M.J., Caves, J.K., Chamberlain, C.P., 2015. A mechanistic analysis of early eocene latitudinal gradients of isotopes in precipitation. Geophys. Res. Lett. 42, 8216–8224. https://doi.org/10.1002/2015GL064829.
Winnick, M.J., Chamberlain, C.P., Caves, J.K., Welker, J.M., 2014. Quantifying the isotopic "continental effect.". Earth Planet. Sci. Lett. 406, 123–133. https://doi.org/10.1016/j.epsl.2014.09.005.
Yang, Y., Roderick, M.L., Zhang, S., McVicar, T.R., Donohue, R.J., 2019. Hydrologic implications of vegetation response to elevated CO_2 in climate projections. Nat. Clim. Chang. 9, 44–48. https://doi.org/10.1038/s41558-018-0361-0.
Yatagai, A., Yasunari, T., 1998. Variation of summer water vapor transport related to precipitation over and around the arid region in the interior of the Eurasian continent. J. Meteorol. Soc. Japan 76, 799–815.
Zanazzi, A., Kohn, M.J., MacFadden, B.J., Terry, D.O., 2007. Large temperature drop across the Eocene-Oligocene transition in central North America. Nature 445, 639–642. https://doi.org/10.1038/nature05551.
Zhang, Xuejun, Tang, Q., Zhang, Xuezhen, Lettenmaier, D.P., 2014. Runoff sensitivity to global mean temperature change in the CMIP5 Models. Geophys. Res. Lett. 41, 5492–5498. https://doi.org/10.1002/2014GL060382.